

Evidence for π -shifted Cooper quartets and few-mode transport in PbTe nanowire three-terminal Josephson junctions

Mohit Gupta,¹ Vipin Khade,¹ Colin Riggert,¹ Lior Shani¹, Gavin Menning,¹ Pim Lueb,² Jason Jung,² Régis Mélin,³ Erik P. A. M. Bakkers,² and Vlad S. Pribiag^{1*}

¹School of Physics and Astronomy, University of Minnesota, Minneapolis, Minnesota 55455, USA

²Department of Applied Physics, Eindhoven University of Technology, Eindhoven, The Netherlands

³Université Grenoble-Alpes, CNRS, Grenoble INP, Institut NEEL, Grenoble, France

*To whom correspondence should be addressed; E-mail: vpribiag@umn.edu.

Abstract

Josephson junctions are typically characterized by a single phase difference across two superconductors. This conventional two-terminal Josephson junction can be generalized to a multi-terminal device where the Josephson energy contains terms with contributions from multiple independent phase variables. Such multi-terminal Josephson junctions (MTJJs) are being considered as platforms for engineering effective Hamiltonians with non-trivial topologies, such as Weyl crossings and higher-order Chern numbers. This approach offers unique possibilities that are complementary to phenomena attainable in bulk crystals, including topological states in more than three dimensions and real-time gate-tunability of the Hamiltonians. However, these prospects rely on the ability to create MTJJs with non-classical multi-terminal couplings in which only a handful of quantum modes are populated. Here, we demonstrate these requirements by using a three-terminal Josephson junction fabricated on selective-area-grown (SAG) PbTe nanowires. We observe signatures of a π -shifted Josephson effect, consistent with inter-terminal couplings mediated by four-particle quantum states called Cooper quartets. We further observe supercurrent co-existent with a non-monotonic evolution of the conductance with gate voltage, indicating transport mediated by a few quantum modes in both two- and three-terminal devices. These results establish a platform for investigations of topological Hamiltonians based on Andreev bound states.

INTRODUCTION

Hybrid superconductor-semiconductor Josephson devices offer a promising path to engineering tunable quantum matter because they combine intrinsic quantum correlations and coherence (stemming from the superconductor) with precise local electrostatic control of the Josephson coupling, number of populated quantum modes and scattering properties (owing to their simultaneous semiconducting character). Superconductivity across the semiconductor is mediated by Andreev bound states (ABS) [1–3], which result from the coherent Andreev reflection of electron-like and hole-like particles at the superconductor-semiconductor interfaces. In general, the Josephson energy of a junction with N -terminals contains $N - 1$ independent phase differences. The ABS of such multi-terminal Josephson junctions (MTJJs) can theoretically provide a means to realize and tune Bloch-like Hamiltonians with non-trivial topology, including Weyl crossings and higher-order Chern numbers [4–8]. However, the realization of these effective Hamiltonians requires multiple superconducting electrodes to be non-classically coupled across a single scattering region and the number of conductance modes connecting the superconducting terminals must be close to unity [4, 5, 9], which has to date proven challenging.

Recent attempts to realize gate-tunable MTJJs have focused on two-dimensional electron systems, such as graphene or III-V semiconductor quantum wells (e.g. InAs) [10–16]. In these devices, the multi-terminal couplings are negligible compared to the two-terminal couplings and the transport properties can thus be explained by a classical network of two-terminal Josephson junctions. The absence of non-classical multi-terminal couplings in these studies is likely due to the extended planar geometries imposed by the two-dimensional materials and the resulting absence of a compact central scattering region. Due to the absence of non-classical inter-terminal couplings, such device geometries are unlikely to realize multi-terminal ABS and topological Hamiltonians. To address this challenge, here we investigate MTJJs based on semiconductor nanowires, which cross in a single central region. The semiconductor platform consists of selective-area-grown (SAG) PbTe nanowires. The nanowires can be grown along multiple crystallographic directions [17] and allow for the nanofabrication of MTJJs where the natural quantum confinement resulting from the wire cross-section at the point of intersection facilitates coherent coupling of multiple superconducting electrodes in a central scattering region.

It was recently theorized that harmonic contributions with π -shifted phase should be present in the current-phase relation of MTJJs with non-classical inter-terminal couplings. This π -shift results from phase-coherent four-particle processes involving all three terminals, called Cooper quartets [18–22]. We observe signatures of π -shifted supercurrent in the diffraction pattern, in the form of an enhanced critical current for small magnetic fields [23–26], along with characteristic differential resistance maps in the space of bias currents. Our results open up a new facile path to fabricate compact multi-terminal Josephson devices with an arbitrary number of terminals and tunable couplings. These devices may have applications ranging from constructing topologically nontrivial Hamiltonians in N -dimensional phase space [4–8] to multi-signal intermodulation which can be used as a building block for neuromorphic computing [16, 27].

Semiconductor nanowires coupled with superconductors are also a leading candidate system for studying Majorana zero modes (MZMs) [28–30], which are predicted non-Abelian states [31, 32]. One of the leading challenges toward the realization of MZMs in nanowire devices to date has been disorder [33–39]. Recently, PbTe semiconducting nanowires have gained attention as an alternative material platform to realize MZMs, with the expectation that the large dielectric constant of PbTe (~ 1000 in bulk) may help screen disorder [40, 41]. PbTe nanowires have the other necessary ingredients for realizing MZMs, such as large g -factors and spin-orbit coupling [17, 42, 43]. Recently, ballistic one-dimensional transport [44–46] and induced superconductivity [47, 48] have been achieved in PbTe SAG nanowires. However, demonstration of few mode transport coexistent with induced superconductivity is lacking. In our work, we observe plateau-like conductance features co-existent with supercurrent in both two- and three-terminal devices, indicating superconductivity in the regime of few quantum modes.

The combination of ballistic supercurrent in the few-modes regime and π -shifted quartets demonstrated here, establishes PbTe SAG as a promising material system for the exploration of MTJJ topological ABS and MZMs that addresses major challenges of other platforms through simultaneous disorder mitigation, geometrical confinement, and as-grown, potentially scalable, desired geometries.

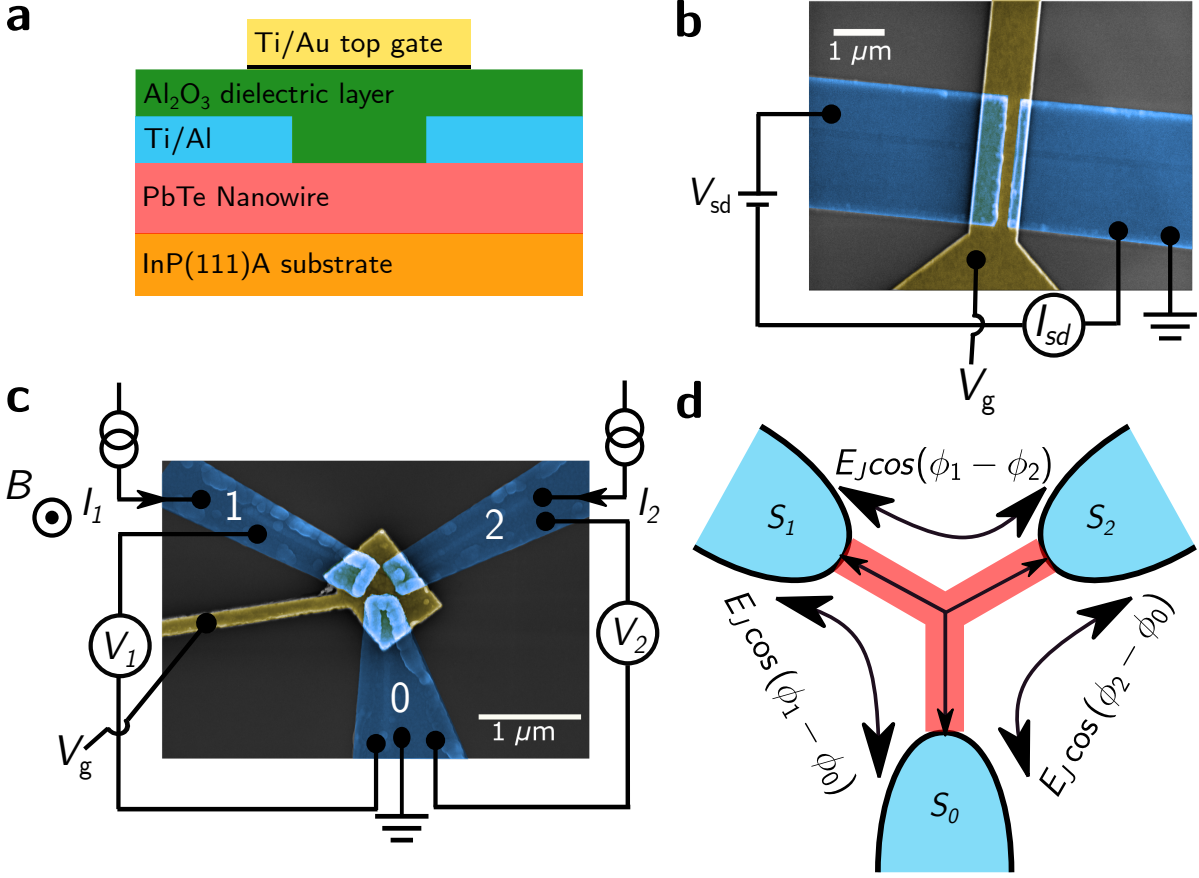


Figure 1. **Device schematics.** **a**, Cross-sectional schematic of the device material stack (not to scale). **b**, False-color scanning electron microscope (SEM) image of a two-terminal Josephson junction. **c**, SEM image of a three-terminal MTJJ (Device 4) along with measurement schematics used for the measurements on Device 3. The blue region corresponds to the superconducting electrodes and gold with the electrostatic gate. PbTe wires are visible underneath the Al electrodes. **d**, Schematic of transport in a three-terminal MTJJ, showing Josephson couplings between pairs of contacts. Terms corresponding to multi-terminal couplings are not displayed.

RESULTS

Device architecture

The PbTe nanowire synthesis is discussed in Supplementary Information Section I. Device contacts are deposited by evaporating either Ti/Al (superconducting contacts) or Ti/Au (normal contacts). Electrostatic control is enabled by metallic top gates with AlO_x gate di-

electric, resulting in the stack structure shown in Figure 1a. Scanning electron microscope (SEM) images of two- and three-terminal Josephson junctions (3TJJs), along with measurement schematics, are shown in Figure 1b and c respectively. Two-terminal devices are measured in the voltage-bias configuration and three-terminal devices are measured in the current-bias configuration unless otherwise specified. The spacing between superconducting electrodes is measured to be ~ 150 nm for two-terminal devices and ~ 250 nm for three-terminal devices. We present four devices in this work, labeled Device 1 – 4.

We begin by discussing the results of two-terminal devices (Device 1 and Device 2), demonstrating conductance quantization with Ti/Au contacts and induced superconductivity with Ti/Al contacts, respectively. We then focus on results from a three-terminal device (Device 3) and discuss magnetic field diffraction patterns and differential resistance maps as a function of two bias currents, I_1 and I_2 . We then discuss superconducting transport in the few-mode regime between a pair of terminals of a second three-terminal device (Device 4).

Ballistic transport and induced superconductivity

Device 1 uses Ti/Au contacts (see Supplementary Fig. 2a for the device image). The device is measured in a voltage bias configuration of the type shown in Figure 1b, in a dilution refrigerator, at the base temperature of ~ 8 mK. We characterize the conductance of this device as a function of gate voltage V_g and V_{bias} , where $V_{\text{bias}} = V_{\text{sd}} - I_{\text{sd}} * R_{\text{series}}$, with V_{sd} being the source-drain voltage bias, I_{sd} the measured source-drain current, and R_{series} includes the resistance of the low-pass filters, the transimpedance amplifier and the contact resistance. We observe conductance steps for the first few modes, at zero magnetic field, in this device with a 200 nm gate-defined channel. The diamonds of quasi-uniform conductance in the V_g vs. V_{bias} map are visible in Figure 2a. Linecuts at fixed V_{sd} , shown in Figure 2b, confirm these to correspond to the 1, 2, and 3 G_0 quantized conductance plateaus associated with the first three spin-degenerate subbands (with $G_0 = 2e^2/h$, where e is the elementary charge and h the Planck constant). This zero-field conductance quantization is consistent with recent results published on PbTe SAG wires grown on CdTe [44–46]. Zero-field quantized conductance, as seen in this device, is an important milestone towards realizing MZMs in nanowires, as the transition to topological superconductivity requires few-mode ballistic

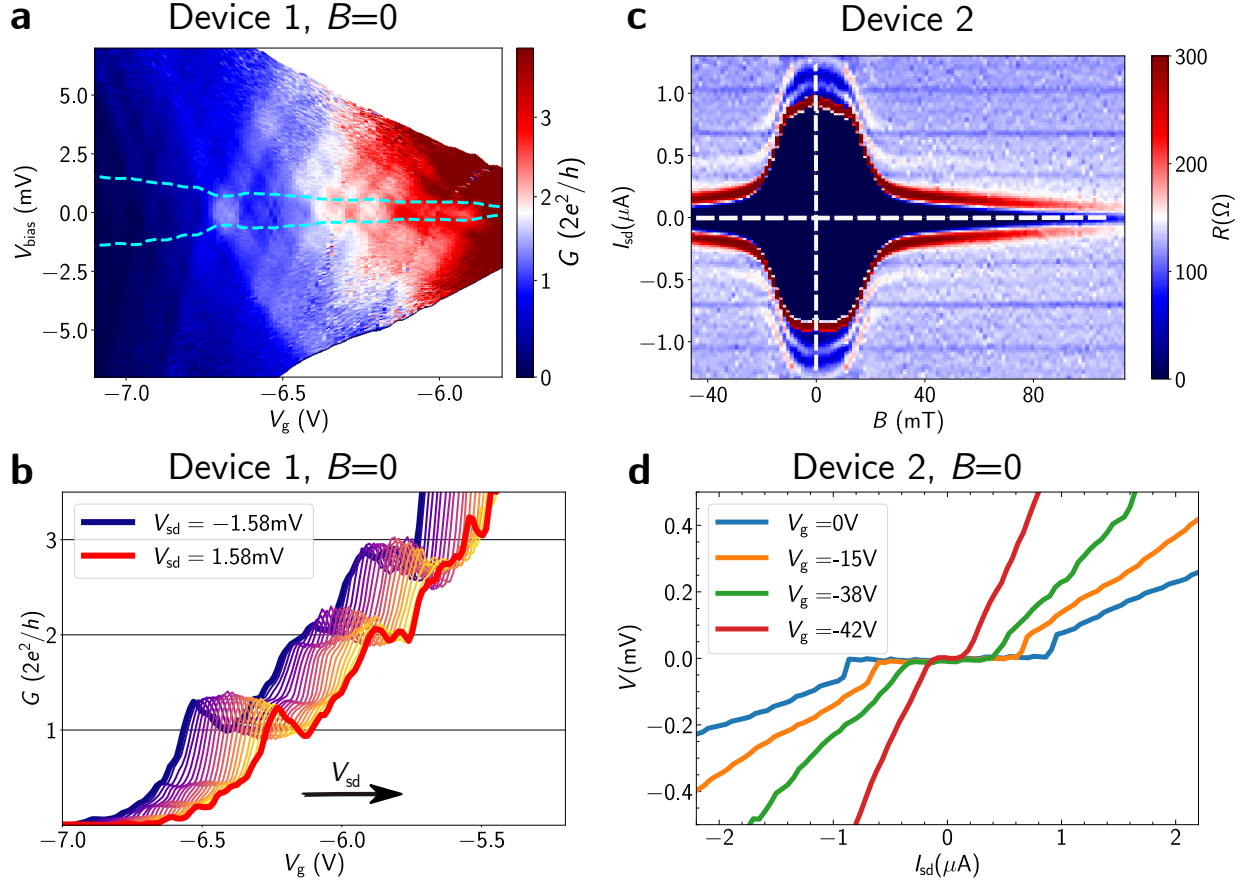


Figure 2. **Ballistic transport characteristics in two-terminal devices.** **a**, Conductance as a function of V_{bias} and V_{g} for Device 1 at $B = 0$. **b**, Conductance as a function of V_{g} for different V_{sd} for Device 1 at $B = 0$. The curves correspond to V_{sd} values between -1.58 mV and 1.58 mV (shown by dashed cyan lines in panel **a**) in increments of 0.150 mV. The curves are each offset along the V_{g} axis for clarity with an arrow indicating the direction of increasing V_{sd} . **c**, R as a function of I_{sd} and B for Device 2, dashed white lines show zero of B and I_{sd} . **d**, $I - V$ characteristics for different values of V_{g} for Device 2.

transport and fields of only a few hundreds of mT [28, 29, 34]. Additionally, zero-field quantized conductance is qualitatively suggestive of low levels of device disorder[49], the importance of which has been stressed in recent theoretical studies of MZMs in realistic device architectures, which suggest that disorder is the largest impediment in the clear observation of MZMs in nanowires [28, 35, 36].

We have also performed conductance measurements at high magnetic fields and elevated temperatures, which further support the claim of conductance quantization in Device 1 (See

Supplementary Information section II and Supplementary Fig. 2.) Several checkerboard-like resonances are superimposed on the conductance data (Figure 2a and Supplementary Fig. 2). These are consistent with an accidental gate-tunable quantum dot present in these nanowires [43].

Having discussed the normal state transport, we now characterize the superconducting properties of a two-terminal device with Ti/Al contacts (Device 2). We first set V_g to a value of 0 V. Upon subtraction of R_{series} , the device resistance, $R = dV_{\text{sd}}/dI_{\text{sd}} - R_{\text{series}}$, is obtained as a function of I_{sd} and the applied out-of-plane magnetic field, B (Figure 2c). The observed diffraction pattern has only one central lobe, consistent with one-dimensional supercurrent flow in this 100nm diameter wire. We also observe Fiske resonances [50] above the zero resistance region in the central lobe, indicating a well-defined Josephson cavity. A similar diffraction pattern is observed as a function of the in-plane magnetic field (Supplementary Fig. 3a), further confirming the one-dimensional nature of supercurrent flow. We have also measured Josephson junctions with different wire diameters, down to a minimum of 60 nm (see Supplementary Fig. 3b, c), showing good reproducibility. Tuning V_g to negative values reduces the switching current (I_s) and increases the normal state resistance, showing induced gate-tunable superconductivity (Figure 2d). Somewhat large electric fields (corresponding to $V_g \sim -40V$) are required to observe an appreciable change in the critical current of this device. This could be due to unintentional higher levels of Pb in some of the nanowires from growth, or other unknown wire non-idealities.

Three-terminal Josephson junctions

We now turn our attention to the three-terminal Josephson junctions. To map out their phase diagrams, two bias currents, I_1 and I_2 , are varied, and two voltages, V_1 and V_2 , are measured (see Figure 1c for measurement schematic), resulting in differential resistance maps, as shown in Figure 3a for Device 3. We observe three superconducting arms in the differential resistance maps along with a central superconducting feature. The superconducting arms are roughly along $I_1 = I_2$, $I_1 = -2I_2$ and $I_2 = -2I_1$ (see Supplementary Fig. 4a for the full dataset). In the central superconducting region, at $B = 0$, superconductivity appears to be split into two distinct pockets at a finite value of I_2 separated by regions of finite resistance. Importantly, when both currents are set to zero, we observe a finite differ-

ential resistance as shown by the non-zero slope of $I_1 - V_1$ curve at $I_2 = 0$ in Figure 3b. At finite I_2 , we observe regions of constant V_1 (indicated by arrows in Figure 3b), yielding zero differential resistance. V_1 values are corrected for the offset due to the instruments and the series resistance due to the contacts. Such features in the central superconducting region have not been observed in previous MTJJ experiments. In the presence of π -supercurrent, the critical current can be vanishing at $B = 0$ [23–26]. The observation of finite differential resistance near zero current biases with vanishing differential resistance at finite I_2 -bias suggests the presence of π -supercurrent in our device, stemming from multi-terminal coherent processes [18–22].

To further clarify this point, we performed magnetic field measurements at fixed values of I_2 , sweeping I_1 and varying the out-of-plane magnetic field, B . For $I_2 = 0$, the resulting interference patterns on these devices show a non-convex pattern, i.e. critical current increases with magnetic field for small B , as can be seen in Figure 3c in the transition from the superconducting state to the normal state. At $I_1 \sim 0$, a feature with finite differential resistance is present that converges toward $I_1 = 0$ near $B = 0$. Such non-convex diffraction patterns in two-terminal devices have been interpreted as a signature of the $0 - \pi$ Josephson current-phase relation ($C\varphi R$) [23–26], further suggesting the existence of π supercurrent contribution in our device.

To understand the transport properties of the differential resistance map and $0 - \pi$ supercurrent, we model our device’s Josephson energy including terms corresponding to both the usual two-terminal process, with energy E_J , and a three-terminal process, with energy E'_J , as shown in Equation 1. In the presence of only the two-terminal process, the device can be modeled as a semi-classical resistively and capacitively shunted junction (RCSJ) network model, as discussed in Refs. [12, 14]. The superconducting arms in the phase diagram appear when a single Josephson junction present between any pair of terminals is superconducting. The slopes of these superconducting arms in the I_1 - I_2 plane can be understood by the resistor network model presented in Refs. [12, 14, 16].

$$\begin{aligned}
 E = & -E_J \cos(\phi_1 - \phi_0) - E_J \cos(\phi_2 - \phi_0) - E_J \cos(\phi_1 - \phi_2) \\
 & -E'_J \cos(\phi_1 + \phi_0 - 2\phi_2) - E'_J \cos(\phi_2 + \phi_0 - 2\phi_1) - E'_J \cos(\phi_1 + \phi_2 - 2\phi_0)
 \end{aligned} \tag{1}$$

However, the central superconducting feature and the non-convex interference pattern cannot be captured by this RCSJ network model. To fit the observed interference pattern,

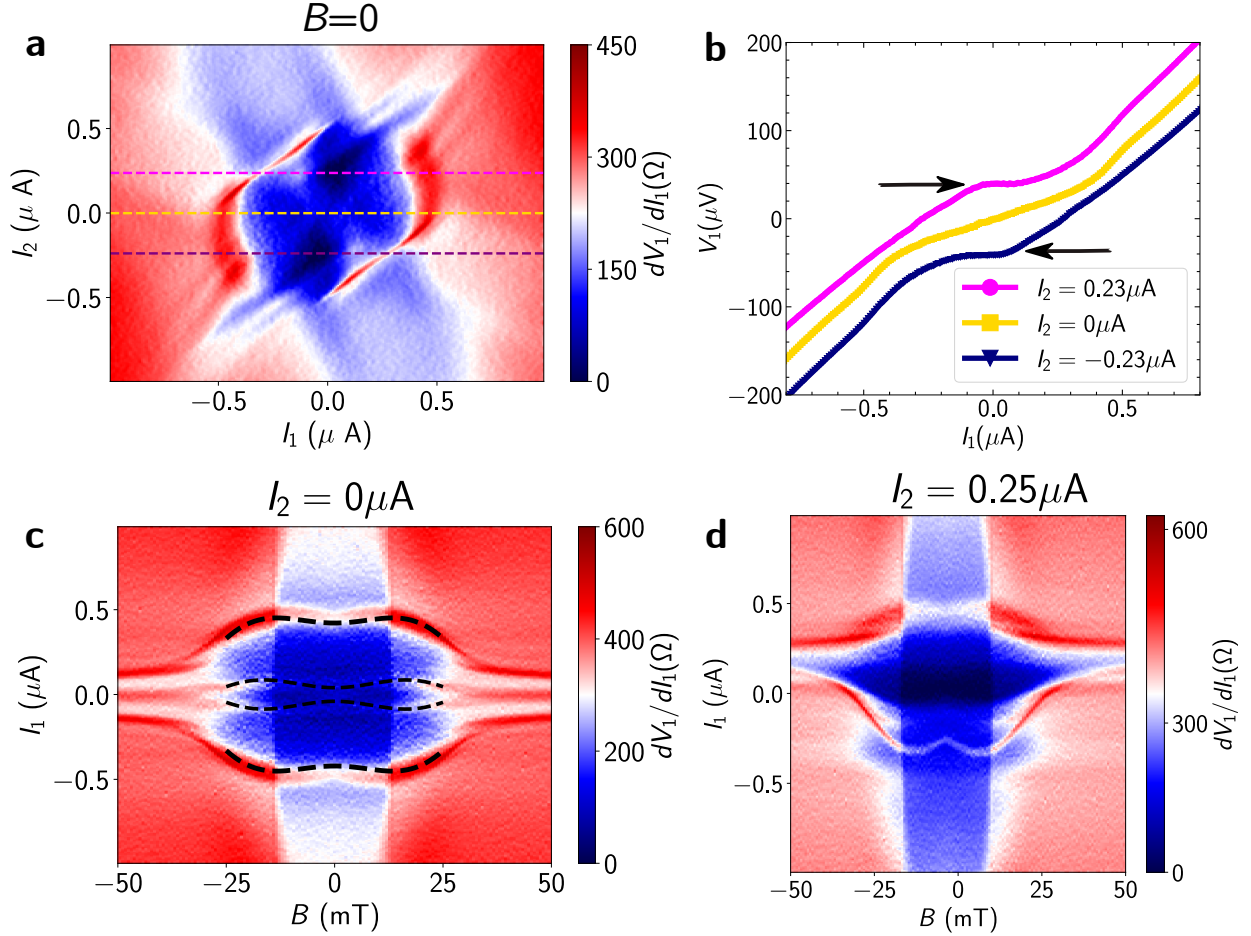


Figure 3. **Three-terminal transport** **a**, Differential resistance map as a function of bias currents I_1 and I_2 for Device 3 at $B = 0$. **b**, $I_1 - V_1$ characteristics for different values of I_2 shown by dashed lines in **a**. The curves are offset vertically for clarity by $40 \mu\text{V}$, $0 \mu\text{V}$ and $-40 \mu\text{V}$ for $I_2 = 0.23 \mu\text{A}$, $I_2 = 0 \mu\text{A}$ and $I_2 = -0.23 \mu\text{A}$, respectively. Arrows indicate the region of vanishing differential resistance. **c**, **d**, Differential resistance as a function of B and bias current I_1 at $I_2 = 0$ and $I_2 = 0.25 \mu\text{A}$, respectively. The dashed black lines in **c** show the fit to the π -shifted quartet model.

we derive an expression for the critical current, I_c as a function of the magnetic field by starting from the expression for the total Josephson energy of the device, Equation 1. The π -shifted $C\varphi R$ sets $E'_J < 0$ [19]. Gauge-invariance and the applied magnetic field allow us to write, $\phi_1 - \phi_0 = \frac{2\pi BA}{\phi_e} = \Phi$, where B is the applied magnetic field, A is the junction area and ϕ_e is the flux quantum. We arrive at the following expression for the critical current as a function of magnetic field (See Supplementary Information section V for the full model

derivation) for small magnetic fields and small E'_J :

$$I_c(\Phi) = \frac{4e}{\hbar} |E_J \cos(\Phi/2) + E'_J \cos(3\Phi/2)| \quad (2)$$

We fit Equation 2 to the non-convex feature present at $I_1 \sim 0.5\mu\text{A}$ in our experimental data and obtain the curve shown in Figure 3c by a dashed black line, with $E_J = 0.26\frac{\hbar}{2e}\mu\text{A}$ and $E'_J = -0.05\frac{\hbar}{2e}\mu\text{A}$ and $A = 0.029\mu\text{m}^2$. The good agreement between our experiment and theory serves as compelling evidence for the presence of quartet transport due to correlated Cooper pairs across the three superconducting terminals. The finite differential resistance feature that converges toward $I_1 = 0$ near $B = 0$ can also be fitted with the same equation. This is fitted with $E_J = 0.04\frac{\hbar}{2e}\mu\text{A}$ and $E'_J = -0.02\frac{\hbar}{2e}\mu\text{A}$ and $A = 0.035\mu\text{m}^2$. The fit is shown by thin dashed black lines converging towards $I_1 = 0$ in Figure 3c. The values of A differ from the lithographically defined dimensions, which can be attributed to flux focusing effects [51–53].

Next, we study the quantum interference patterns for $I_2 \neq 0$. For positive (negative) values of I_2 , the non-convex diffraction pattern appears only for the negative (positive) value of I_1 and remains flat for positive (negative) values of I_1 (Figure 3d and Supplementary Fig. 4b). This shows that the current bias via terminal 2 can be used as another knob for tuning the phase differences, in addition to the applied field, resulting in non-reciprocal π -supercurrent (i.e. a superconducting diode effect) flow. Our current model does not consider these processes and hence we have not fitted any theoretical curve to these data. In addition, the center of the interference pattern is shifted along the I_1 axis. This shift is simply a consequence of current conservation.

Few-mode superconducting transport in 3TJJs

The superconducting devices discussed so far required relatively large negative gate voltages to modulate conductance and could not be safely pinched off. However, from the same material growth batch, there are devices on which complete pinch-off of the channel is observed (both two- and three-terminal devices). We demonstrate few-mode transport co-existent with superconductivity on a three-terminal device (Device 4). Figure 4a shows the conductance map for a pair of terminals as a function of V_{sd} and V_g for Device 4. When the device is superconducting, the voltage drop across the device vanishes, resulting in

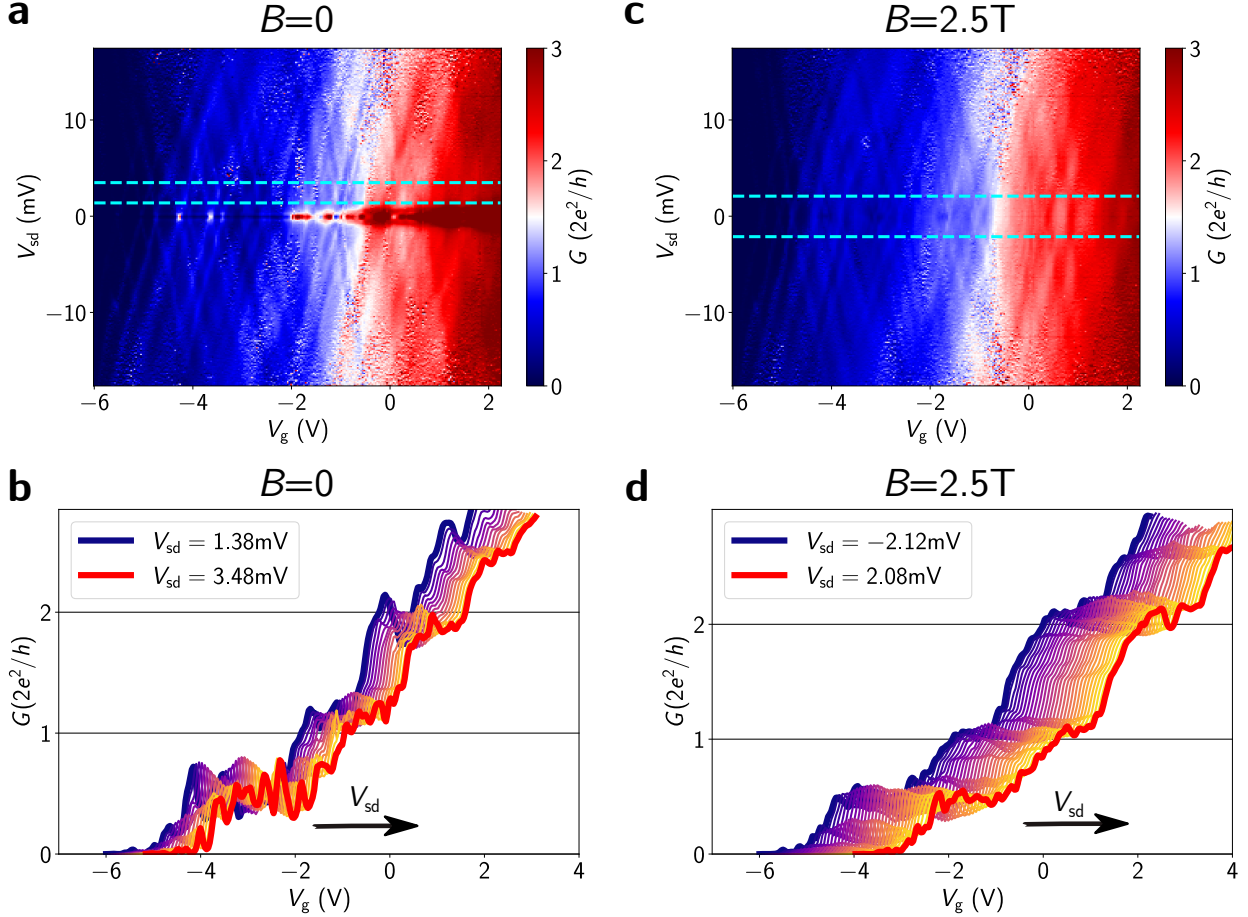


Figure 4. **Superconducting transport in the few-modes regime.** **a, c,** Conductance as a function of source-drain bias, V_{sd} , and gate voltage, V_g , for Device 4 at $B = 0\text{T}$ and $B = 2.5\text{T}$, respectively. **b, d,** Conductance as a function of gate voltage for different V_{sd} at $B = 0\text{T}$ and $B = 2.5\text{T}$, respectively. The curves correspond to V_{sd} values of 1.38 mV to 3.48 mV (panel **b**) and -2.12 mV to 2.08 mV (panel **d**), shown by the dashed cyan lines in **a** and **c**. The curves are each offset along the V_g axis for clarity. Arrows indicate the direction of increasing V_{sd} .

$V_{sd} = I_{sd} \times R_{\text{series}}$. Critical current contours are thus observed as areas of high conductance or zero resistance for small bias. Plateau-like conductance features are seen at higher bias values as a function of V_g (Figure 4b), with superimposed conductance oscillations. The oscillations could be due to Fabry-Pérot interference or an accidental quantum dot present in the wire [14, 54, 55]. The plateau features are not quantized in multiples of G_0 . This is likely due to the high source-drain bias. At finite bias, the value of the conductance steps is determined by the number of quasi-1D subbands falling within the bias window set by

V_{sd} [56–59]. It is not possible to perform zero bias conductance quantization measurements on a Josephson device as the device is superconducting at $V_{sd} = 0$. Similar results were reproduced on a two-terminal Josephson device (Supplementary Fig. 5). Taken together, the presence of this non-monotonic, plateau-like conductance behavior at above-gap bias values, along with supercurrent at lower bias, indicate few-mode operation of these superconducting nanowire devices. This is one of the necessary conditions for the observation of Weyl nodes in the ABS of MTJJs and the detection of MZMs in two-terminal devices.

To further characterize the ballistic few-mode transport in Device 4 we apply a 2.5 T out-of-plane magnetic field to drive the device from the superconducting to normal state and again perform DC measurements as a function of V_g and V_{sd} . The resulting data, plotted in Figure 4c, shows diamond-shaped regions of approximately uniform conductance. Linecuts of this data, shown in Figure 4d, show better-defined conductance plateau features with reduced conductance oscillations, attributed to the suppression of coherent backscattering due to the Aharonov-Bohm phase contribution. The plateau features become aligned with multiples of $0.5 G_0$ at low bias, consistent with Zeeman-split subbands. This evolution to half-quantization under applied field further strengthens the interpretation of few-mode transport at zero field.

We note that out of the three pairs of terminals on this device, two pairs showed few-mode transport, while the third pair showed similar behavior to Device 2, where large electric fields were needed to pinch off the device. We also observed checkerboard conductance features superimposed on the conductance map, similar to those seen for Device 1. Such features, attributed to accidental quantum dots, are observed in all devices that show depletion of the scattering region for reasonable values of gate voltage ($V_g \sim 6V$). We resolve these quantum dot features in Device 4 by exploring the low conductance region (Supplementary Information section VI and Supplementary Fig. 6). We find results consistent with previous characterizations of quantum dots on PbTe, such as near-zero charging energy and large anisotropic g-factors [17, 43].

DISCUSSION

In summary, we report experimental evidence of π -shifted supercurrents in three-terminal Josephson junctions, consistent with substantial non-classical multi-terminal coupling via

quartets. To our knowledge, there has been no prior experimental detection of π -shifted quartets. Other resonant features in the differential resistance maps of MTJJs, obtained in the non-equilibrium regime [60, 61], can also point to quartet processes, however in such cases the experimental features can also be due to correlated phase dynamics in a classical circuit in the RCSJ picture [14, 15], and thus may not necessarily be due to quartets.

As further confirmation of our analysis, we consider alternative explanations that could give rise to the observed non-convex patterns, i.e. field enhanced critical currents. These include quasiparticle cooling effects [62], magnetic-impurities [63] and flux pinning [64]. Quasiparticle-mediated cooling would give rise to hysteretic critical currents and should show enhancement of the critical current with in-plane magnetic fields. In contrast, the observed diffraction pattern in our work is symmetric in current and we do not observe the enhancement of the critical current under applied in-plane magnetic field, as can be seen in Supplementary Fig. 7. Furthermore, the SAG nature of the wires is expected to allow for better thermalization of the Josephson junctions via substrate phonons than in the case of transferred wires [62]. Hence, quasiparticle cooling effects are unlikely to cause the non-convex diffraction pattern observed here. Magnetic impurities and flux vortex pinning effects, if present, should be equally effective for two- and three-terminal Josephson junctions made on the same chip using the same fabrication recipe. Yet, the characteristic non-convex MTJJ diffraction pattern from Figure 3 is absent from all of the measured two-terminal devices. Hence, these effects are unlikely to be relevant here.

The addition of superconducting loops, split-gates, and more terminals can allow for custom tuning of the π supercurrent. Our work shows experimentally that MTJJs allow for the creation of π junctions without any magnetic elements in the junction area, greatly simplifying potential applications. Among such use cases, super-semi MTJJ π junctions could enable gate-tunable superconducting neuromorphic circuits or compact superconducting supercomputing applications [16, 65, 66]. In addition, the observed few-quantum-mode transport at zero magnetic field coexisting with superconductivity demonstrates the potential of PbTe SAG nanowires for topological MTJJ devices and for studies of MZMs. Currently, the presence of accidental quantum dots may pose challenges for clean MZM experiments. We expect that further improvements in material growth could mitigate these challenges.

METHODS

Device fabrication

Electrodes were patterned using standard electron beam lithography (EBL) techniques using a tri-layer resist stack with two layers of 4 wt% 495K poly(methyl methacrylate) (PMMA A4) and a single PMMA A2 layer. In-situ ion-mill etch was performed before the evaporation of superconducting Ti/Al (5/50 nm) or normal Ti/Au contacts in a UHV system. Approximately 40 nm of Al₂O₃ dielectric was deposited using thermal atomic layer deposition (ALD). Using EBL, gates were defined over the junction area using the same resist stack that was used for contacts, and electrodes were deposited using electron-beam evaporation of Ti/Au (5 nm/80 nm).

Measurement details

Resistance data on Device 1 and Device 2, differential resistance maps on Device 4, and conductance quantization data on Device 2 were obtained by low-noise DC transport measurements in a ³He/⁴He dilution refrigerator. For the conductance quantization data on Device 3, standard low-frequency lock-in techniques were used with a small excitation voltage and a frequency of 19 Hz. For all the voltage bias measurements, the raw data is corrected by subtracting the series filter and the ammeter resistances ($\sim 7.8\text{k}\Omega$ for Device 1, $\sim 9.7\text{k}\Omega$ for Device 4 and gate sweeps for Device 2, and $\sim 8.8\text{k}\Omega$ for the magnetic field sweep for Device 2). Low-pass Gaussian filtering was used to smooth numerical derivatives. We have subtracted a contact resistance of $6.2\text{k}\Omega$ for Device 1, 100Ω for Device 2, and 120Ω for the leg biased with I_1 and 132Ω for the leg biased with I_2 for Device 3. For Figure 3b we have also subtracted an instrument offset of $44\mu\text{V}$. No subtraction of contact resistance is done for Device 4.

DATA AND CODE AVAILABILITY

Source data for the figures presented in this paper and the data plotting code are available at the following Zenodo database <https://zenodo.org/records/11042066>.

- [1] Meissner, H. Superconductivity of contacts with interposed barriers. *Phys. Rev.* **117**, 672–680 (1960).
- [2] Josephson, B. Possible new effects in superconductive tunnelling. *Phys. Lett.* **1**, 251–253 (1962).
- [3] Anderson, P. W. & Rowell, J. M. Probable observation of the josephson superconducting tunneling effect. *Phys. Rev. Lett.* **10**, 230–232 (1963).
- [4] Riwar, R. P., Houzet, M., Meyer, J. S. & Nazarov, Y. V. Multi-terminal Josephson junctions as topological matter. *Nat. Commun.* **7**, 11167 (2016).
- [5] J. S. Meyer & Houzet, M. Nontrivial Chern Numbers in Three-Terminal Josephson Junctions. *Phys. Rev. Lett.* **119**, 136807 (2017).
- [6] Xie, H. Y., Vavilov, M. G. & Levchenko, A. Topological Andreev bands in three-terminal Josephson junctions. *Phys. Rev. B* **96**, 161406(R) (2017).
- [7] Xie, H. Y., Vavilov, M. G. & Levchenko, A. Weyl nodes in Andreev spectra of multiterminal Josephson junctions: Chern numbers, conductances, and supercurrents. *Phys. Rev. B* **97**, 035443 (2018).
- [8] Xie, H.-Y., Hasan, J. & Levchenko, A. Non-abelian monopoles in the multiterminal josephson effect. *Phys. Rev. B* **105**, L241404 (2022).
- [9] Eriksson, E., Riwar, R.-P., Houzet, M., Meyer, J. S. & Nazarov, Y. V. Topological transconductance quantization in a four-terminal josephson junction. *Phys. Rev. B* **95**, 075417 (2017).
- [10] Draelos, A. W. *et al.* Supercurrent Flow in Multiterminal Graphene Josephson Junctions. *Nano Lett.* **19**, 1039–1043 (2019).
- [11] Pankratova, N. *et al.* Multiterminal josephson effect. *Phys. Rev. X* **10**, 031051 (2020).
- [12] Graziano, G. V., Lee, J. S., Pendharkar, M., Palmstrøm, C. J. & Pribiag, V. S. Transport studies in a gate-tunable three-terminal josephson junction. *Phys. Rev. B* **101**, 054510 (2020).

- [13] Arnault, E. G. *et al.* Multiterminal inverse ac josephson effect. *Nano Lett.* **21**, 9668–9674 (2021).
- [14] Graziano, G. V. *et al.* Selective control of conductance modes in multi-terminal josephson junctions. *Nat. Commun.* **13**, 5933 (2022).
- [15] Arnault, E. G. *et al.* Dynamical stabilization of multiplet supercurrents in multiterminal josephson junctions. *Nano Lett* **22**, 7073–7079 (2022).
- [16] Gupta, M. *et al.* Gate-tunable superconducting diode effect in a three-terminal josephson device. *Nat. Commun.* **14**, 3078 (2023).
- [17] Jung, J. *et al.* Selective Area Growth of PbTe Nanowire Networks on InP. *Advanced Functional Materials* **32**, 2208974 (2022).
- [18] Freyn, A., Douçot, B., Feinberg, D. & Mélin, R. Production of nonlocal quartets and phase-sensitive entanglement in a superconducting beam splitter. *Phys. Rev. Lett.* **106**, 257005 (2011).
- [19] Mélin, R., Danneau, R. & Winkelmann, C. B. Proposal for detecting the π -shifted cooper quartet supercurrent. *Phys. Rev. Res.* **5**, 033124 (2023).
- [20] Mélin, R. & Feinberg, D. Quantum interferometer for quartets in superconducting three-terminal josephson junctions. *Phys. Rev. B* **107**, L161405 (2023).
- [21] Jonckheere, T. *et al.* Quartet currents in a biased three-terminal diffusive josephson junction. *Phys. Rev. B* **108**, 214517 (2023).
- [22] Mélin, R., Winkelmann, C. B. & Danneau, R. Magnetointerferometry of multiterminal josephson junctions. *Phys. Rev. B* **109**, 125406 (2024).
- [23] Bulaevskii, L., Kuzii, V. & Sobyenin, A. On possibility of the spontaneous magnetic flux in a josephson junction containing magnetic impurities. *Solid State Communications* **25**, 1053–1057 (1978).
- [24] Weides, M. *et al.* $0-\pi$ josephson tunnel junctions with ferromagnetic barrier. *Phys. Rev. Lett.* **97**, 247001 (2006).
- [25] Frolov, S. M., Van Harlingen, D. J., Bolginov, V. V., Oboznov, V. A. & Ryazanov, V. V. Josephson interferometry and shapiro step measurements of superconductor-ferromagnet-superconductor $0-\pi$ junctions. *Phys. Rev. B* **74**, 020503 (2006).
- [26] Kang, K. *et al.* van der Waals π Josephson Junctions. *Nano Lett.* **22**, 5510–5515 (2022).

- [27] Goteti, U. S. & Dynes, R. C. Superconducting neural networks with disordered Josephson junction array synaptic networks and leaky integrate-and-fire loop neurons. *Journal of Applied Physics* **129** (2021).
- [28] Lutchyn, R. M., Sau, J. D. & Das Sarma, S. Majorana fermions and a topological phase transition in semiconductor-superconductor heterostructures. *Phys. Rev. Lett.* **105**, 077001 (2010).
- [29] Oreg, Y., Refael, G. & von Oppen, F. Helical liquids and majorana bound states in quantum wires. *Phys. Rev. Lett.* **105**, 177002 (2010).
- [30] Lutchyn, R. M. *et al.* Majorana zero modes in superconductor-semiconductor heterostructures. *Nat. Rev. Mater.* **3**, 52–68 (2018).
- [31] Kitaev, A. Y. Fault-tolerant quantum computation by anyons. *Ann. Phys. (N.Y.)* **303**, 2–30 (2003).
- [32] Nayak, C., Simon, S. H., Stern, A., Freedman, M. & Das Sarma, S. Non-Abelian anyons and topological quantum computation. *Rev. Mod. Phys.* **80**, 1083–1159 (2008).
- [33] Liu, J., Potter, A. C., Law, K. T. & Lee, P. A. Zero-Bias Peaks in the Tunneling Conductance of Spin-Orbit-Coupled Superconducting Wires with and without Majorana End-States. *Phys. Rev. Lett.* **109**, 267002 (2012).
- [34] Mourik, V. *et al.* Signatures of majorana fermions in hybrid superconductor-semiconductor nanowire devices. *Science* **336**, 1003–1007 (2012).
- [35] Das Sarma, S. & Pan, H. Disorder-induced zero-bias peaks in Majorana nanowires. *Phys. Rev. B* **103**, 195158 (2021).
- [36] Pan, H., Liu, C.-X., Wimmer, M. & Das Sarma, S. Quantized and unquantized zero-bias tunneling conductance peaks in Majorana nanowires: Conductance below and above $2e^2/h$. *Phys. Rev. B* **103**, 214502 (2021).
- [37] Ahn, S., Pan, H., Woods, B., Stanescu, T. D. & Das Sarma, S. Estimating disorder and its adverse effects in semiconductor Majorana nanowires. *Phys. Rev. Mater.* **5**, 124602 (2021).
- [38] Jiang, Y. *et al.* Zero-bias conductance peaks at zero applied magnetic field due to stray fields from integrated micromagnets in hybrid nanowire quantum dots (2023). URL <https://arxiv.org/abs/2305.19970>.
- [39] Frolov, S. M. *et al.* "Smoking gun" signatures of topological milestones in trivial materials by measurement fine-tuning and data postselection (2023). URL <https://arxiv.org/abs/>

2309.09368.

- [40] Huang, Y. & Shklovskii, B. I. Disorder effects in topological insulator nanowires. *Phys. Rev. B* **104**, 054205 (2021).
- [41] Cao, Z. *et al.* Numerical study of PbTe-Pb hybrid nanowires for engineering Majorana zero modes. *Phys. Rev. B* **105**, 085424 (2022).
- [42] ten Kate, S. C. *et al.* Small Charging Energies and g-Factor Anisotropy in PbTe Quantum Dots. *Nano Lett.* **22**, 7049–7056 (2022).
- [43] Gomanko, M. *et al.* Spin and Orbital Spectroscopy in the Absence of Coulomb Blockade in Lead Telluride Nanowire Quantum Dots. *SciPost Phys.* **13**, 089 (2022).
- [44] Song, W. *et al.* Conductance quantization in PbTe nanowires. *Phys. Rev. B* **108**, 045426 (2023).
- [45] Wang, Y. *et al.* Ballistic PbTe Nanowire Devices. *Nano Lett.* **23**, 11137–11144 (2023).
- [46] Song, W. *et al.* Reducing disorder in PbTe nanowires for Majorana research (2024). URL <https://arxiv.org/abs/2402.02132>.
- [47] Zhang, Z. *et al.* Proximity effect in PbTe-Pb hybrid nanowire Josephson junctions. *Phys. Rev. Mater.* **7**, 086201 (2023).
- [48] Li, R. *et al.* Selective-Area-Grown PbTe-Pb Planar Josephson Junctions for Quantum Devices (2023). URL <https://arxiv.org/abs/2311.16815>.
- [49] van Weperen, I., Plissard, S. R., Bakkers, E. P. A. M., Frolov, S. M. & Kouwenhoven, L. P. Quantized conductance in an insb nanowire. *Nano Lett.* **13**, 387–391 (2013).
- [50] Coon, D. D. & Fiske, M. D. Josephson ac and step structure in the supercurrent tunneling characteristic. *Phys. Rev.* **138**, A744–A746 (1965).
- [51] Pribiag, V. S. *et al.* Edge-mode superconductivity in a two-dimensional topological insulator. *Nat. Nanotechnol.* **10**, 593–597 (2015).
- [52] Paajaste, J. *et al.* Pb/InAs nanowire Josephson junction with high critical current and magnetic flux focusing. *Nano Letters* **15**, 1803–1808 (2015).
- [53] Harada, Y., Jensen, S., Akazaki, T. & Takayanagi, H. Anomalous magnetic flux periodicity of supercurrent in mesoscopic SNS Josephson junctions. *Physica C: Superconductivity* **367**, 229–233 (2002).
- [54] Calado, V. E. *et al.* Ballistic Josephson junctions in edge-contacted graphene. *Nat. Nano.* **10**, 761–764 (2015).

- [55] Shani, L. *et al.* Diffusive and ballistic transport in thin InSb nanowire devices using a few-layer-graphene-AlOx gate. *Mater. Quantum. Technol.* **4**, 015101 (2024).
- [56] Kouwenhoven, L. P. *et al.* Nonlinear conductance of quantum point contacts. *Phys. Rev. B* **39**, 8040–8043 (1989).
- [57] Patel, N. K. *et al.* Evolution of half plateaus as a function of electric field in a ballistic quasi-one-dimensional constriction. *Phys. Rev. B* **44**, 13549–13555 (1991).
- [58] Gallagher, P., Lee, M., Williams, J. R. & Goldhaber-Gordon, D. Gate-tunable superconducting weak link and quantum point contact spectroscopy on a strontium titanate surface. *Nat. Phys.* **10**, 748–752 (2014).
- [59] Lee, J. S. *et al.* Transport Studies of Epi-Al/InAs Two-Dimensional Electron Gas Systems for Required Building-Blocks in Topological Superconductor Networks. *Nano Lett.* **19**, 3083 (2019).
- [60] Cohen, Y. *et al.* Nonlocal supercurrent of quartets in a three-terminal Josephson junction. *Proc. Natl. Acad. Sci. U.S.A.* **115**, 6991–6994 (2018).
- [61] Huang, K.-F. *et al.* Evidence for $4e$ charge of Cooper quartets in a biased multi-terminal graphene-based Josephson junction. *Nat. Commun.* **13**, 3032 (2022).
- [62] Murani, A. *et al.* Long- to short-junction crossover and field-reentrant critical current in al/ag-nanowires/al josephson junctions. *Phys. Rev. B* **102**, 214506 (2020).
- [63] Rogachev, A. *et al.* Magnetic-field enhancement of superconductivity in ultranarrow wires. *Phys. Rev. Lett.* **97**, 137001 (2006).
- [64] Sato, Y. *et al.* Quasiparticle trapping at vortices producing josephson supercurrent enhancement. *Phys. Rev. Lett.* **128**, 207001 (2022).
- [65] Ortlepp, T. *et al.* RSFQ Circuitry Using Intrinsic π -Phase Shifts. *IEEE Transactions on Applied Superconductivity* **17**, 659–663 (2007).
- [66] Kamiya, T., Tanaka, M., Sano, K. & Fujimaki, A. Energy/Space-Efficient Rapid Single-Flux-Quantum Circuits by Using π -Shifted Josephson Junctions. *IEICE Transactions on Electronics* **E101.C**, 385–390 (2018).

ACKNOWLEDGEMENTS

All aspects of the work at UMN were supported by the Department of Energy under Award No. DE-SC0019274. Portions of this work were conducted in the Minnesota Nano Center, which is supported by the National Science Foundation through the National Nano Coordinated Infrastructure Network (NNCI) under Award Number ECCS-1542202. Eindhoven University of Technology acknowledges the research program “Materials for the Quantum Age” (QuMat) for financial support. This program (registration number 024.005.006) is part of the Gravitation program financed by the Dutch Ministry of Education, Culture and Science (OCW). Eindhoven University of Technology acknowledges European Research Council (ERC TOCINA 834290).

AUTHOR CONTRIBUTIONS

M.G. and V.S.P. designed the experiments. M.G. and V.K. fabricated Devices 1,2 and 4 with help from L.S. M.G. performed the measurements on Devices 1, 2, and 4 and analyzed the data with help from V.K. G.M. and L.S. fabricated Device 3. C.R. performed measurements and analyzed data on Device 3 with help from G.M. P.L. and E.P.A.M.B. provided the nanowires. R.M. provided the theoretical model for the three-terminal device. All authors contributed to writing the manuscript. V.S.P. supervised the project.

COMPETING INTERESTS

The authors declare no competing interests.

Supplementary Information for "Evidence for π -shifted Cooper quartets and few-mode transport in PbTe nanowire three-terminal Josephson junctions"

Mohit Gupta,¹ Vipin Khade,¹ Colin Riggert,¹ Lior Shani¹, Gavin Menning,¹ Pim Lueb,² Jason Jung,² Régis Mélin,³ Erik P. A. M. Bakkers,² and Vlad S. Pribiag^{1*}

¹School of Physics and Astronomy, University of Minnesota, Minneapolis, Minnesota 55455, USA

²Department of Applied Physics, Eindhoven University of Technology, Eindhoven, The Netherlands

³Université Grenoble-Alpes, CNRS, Grenoble INP, Institut NEEL, Grenoble, France

*To whom correspondence should be addressed; E-mail: vpribiag@umn.edu.

I. NANOWIRE GROWTH

PbTe nanowires were grown selectively on an InP(111)A substrate, following the method as outlined in Ref. [1]. A SiN_x mask of 20nm was deposited on an InP(111)A wafer using plasma-enhanced chemical vapor deposition (PECVD). Nanowire patterns were lithographically defined and etched into the mask using a reactive-ion etching (RIE) using CHF₃ with added O₂. The residual resist left over from the lithography step is then chemically removed by ultrasonication in an acetone bath. The substrate is then shortly etched in a phosphoric acid solution (H₂O : H₃PO₄ = 10 : 1) to remove native substrate oxides, after which it is rapidly transferred to the high-vacuum molecular beam epitaxy (MBE) system. Within the MBE system, the samples are degassed at 300°C for 1 hour. Subsequently, samples are annealed at 480°C under a Te overpressure. The temperature is then reduced to 340°C and growth commences under elemental fluxes of Te and Pb, which are 4E-7 mbar and 1.25E-7 mbar, respectively, as determined by a naked Bayard-Alpert ion gauge. The resulting height of the nanowires is ~ 40 nm as measured from the substrate. The resulting wire structures are displayed in Supplementary Fig. 1

II. ADDITIONAL DATA FOR DEVICE 1

The SEM image of the device is shown in Supplementary Fig. 2a, the scattering region is defined by the top gate (shown in pink) with a length of ~ 200 nm. We have performed measurements at high applied magnetic fields and elevated temperatures on Device 1. The obtained conductance maps show diamonds of uniform conductance and linecuts confirm these to be quantized conductance plateaus (Supplementary Fig. 2), consistent with data presented in the main text.

III. ADDITIONAL DATA FOR INDUCED SUPERCONDUCTIVITY

We present additional data on devices similar to the one presented in the main text, Device 2, but with different wire diameters. The observed diffraction patterns are consistent with one dimensional supercurrent flow as there is only one central superconducting lobe with suppression of the second lobe as the wire diameter decreases as seen in Supplementary Fig. 3. The magnitude of critical current also decreases as the wire diameter decreases. This

shows good reproducibility of Josephson device fabrication on this material platform.

IV. ADDITIONAL DATA FOR THREE-TERMINAL DEVICES

We show the full differential resistance map for Device 3 in Supplementary Fig. 4a, showing the full superconducting arms in the I_1 - I_2 plane, displaying the superconducting arms consistent with RCSJ network model. The magnetic field diffraction pattern for $I_2 = -0.25\mu\text{A}$ is shown in Supplementary Fig. 4b. The observed pattern is opposite to what has been observed for $I_2 = 0.25\mu\text{A}$ (Figure 3d). We also show data from a device similar to Device 3, labeled Device 5. Device 5 has a wire diameter of 100nm compared to Device 3 which has a wire diameter of 60nm. Non-convex diffraction pattern and central superconducting feature are also reproduced on this device.

In-plane magnetic field measurement for Device 3 is shown in Supplementary Fig. 7, no field enhancement of critical current is observed, negating self-heating effects.

V. THEORETICAL MODEL

We derive the expression for critical current as a function of magnetic field using the model presented in Ref. [2]. The Josephson energy of a three-terminal device can be written as:

$$E = -E_J \cos(\phi_1 - \phi_0) - E_J \cos(\phi_2 - \phi_0) - E_J \cos(\phi_1 - \phi_2) + \\ -E'_J \cos(\phi_1 + \phi_0 - 2\phi_2) - E'_J \cos(\phi_2 + \phi_0 - 2\phi_1) - E'_J \cos(\phi_1 + \phi_2 - 2\phi_0) \quad (1)$$

If the central area of the device is A then for an applied field B we can write:

$$\phi_0 = -\frac{2\pi BA}{2\phi_e} = -\Phi/2 \\ \phi_1 = \frac{2\pi BA}{2\phi_e} = \Phi/2 \quad (2)$$

Here we have used gauge invariance to set the phase offset between terminal 0 and 1 to be zero. We now arrive at Equation 3:

$$E = -E_J \cos(\Phi) - 2E_J \cos(\Phi/2) \cos(\phi_2) - E'_J \cos(2\phi_2) - 2E'_J \cos(3\Phi/2) \cos(\phi_2) \quad (3)$$

To get an expression for the current-phase relation ($C\varphi R$) we perform derivative w.r.t the free phase variable ϕ_2 :

$$I(\Phi, \phi_2) = \frac{-2e}{\hbar} \frac{\partial E}{\partial \phi_2} = \frac{-2e}{\hbar} (2E_J \cos(\Phi/2) \sin(\phi_2) + 4E'_J \cos(\phi_2) \sin(\phi_2) + 2E'_J \cos(3\Phi/2) \sin(\phi_2)) \quad (4)$$

Maximizing Equation 4 gives the expression for critical current for a given magnetic field. If $E'_J = 0$, then Equation 4 has a maxima at $\phi_2 = \pi/2$ and we recover the usual convex diffraction pattern. For small E'_J we can expand the above expression near $\phi_2 = \pi/2$, with $\phi_2 = \pi/2 + \epsilon$:

$$I(\phi, \epsilon) = \frac{-2e}{\hbar} (2E_J \cos(\Phi/2) - 4E'_J \epsilon + 2E'_J \cos(3\Phi/2)) (1 - \epsilon^2/2) \quad (5)$$

Here we have assumed E'_J and ϵ to be small. Maximizing Equation 5 in ϵ we get the expression for the critical current as:

$$I_c(\Phi) = \frac{4e}{\hbar} (|E_J \cos(\Phi/2) + E'_J \cos(3\Phi/2)|) \quad (6)$$

We have used Equation 6 to fit the observed non-convex diffraction pattern.

VI. QUANTUM DOT CHARACTERIZATION WITH TI/AL CONTACTS

In Supplementary Fig. 5 we show few-mode transport in a two-terminal device. The observed plateau-like features and checkerboard-like resonances are observed in the conductance map in this device similar to Device 1 and 4. All three devices discussed in this work where pinch-off is observed for reasonable values of gate voltage have these resonances present in them likely due to an accidental quantum dot in the nanowire. Such dots are characterized in Device 4 in the range of gate voltage values corresponding to the near pinchoff of the device.

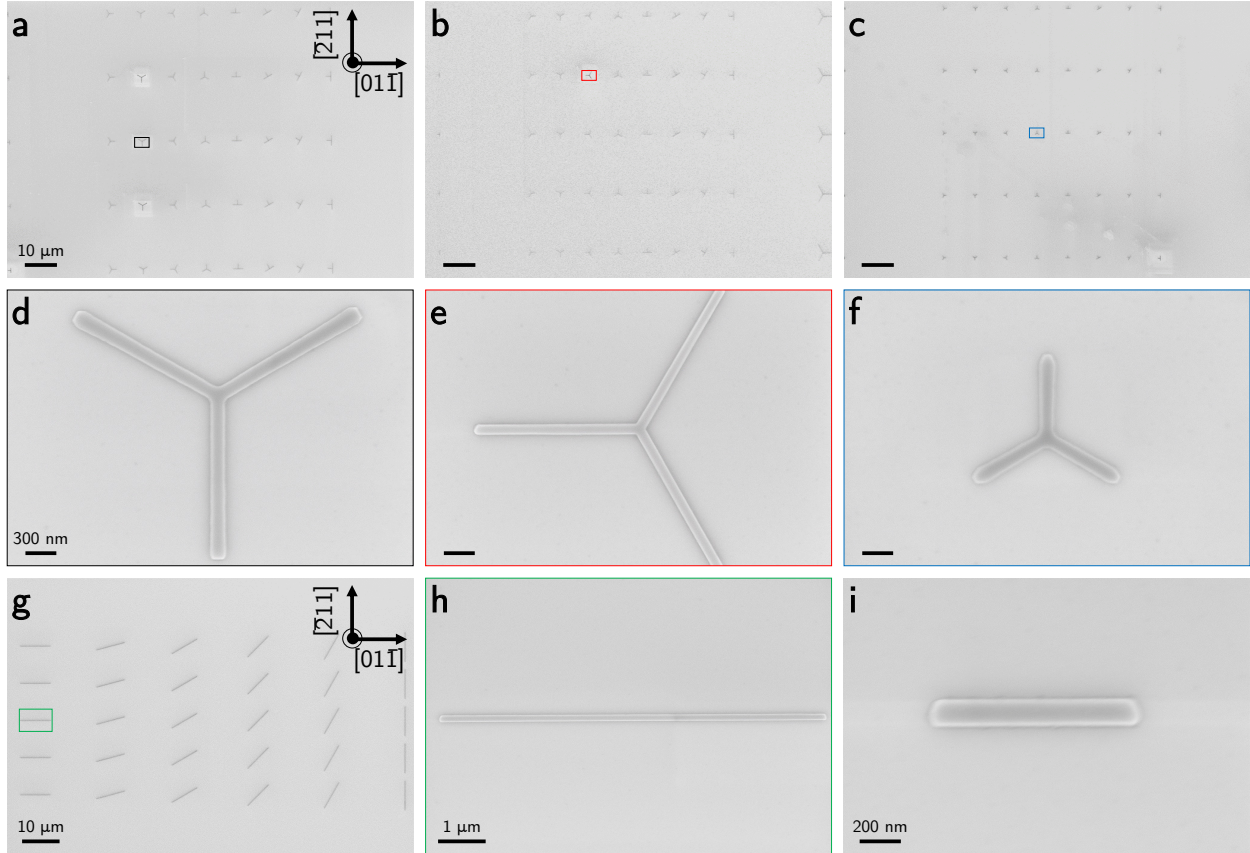
In Supplementary Fig. 6a we observe clearly defined Coulomb diamonds in a bias vs gate charge stability diagram at zero external magnetic field. Upon application of an out-of-plane 2T field, we observe the emergence of additional, smaller diamonds, as shown in Supplementary Fig. 6b. This emergence of additional diamonds with the addition of Zeeman energy, instead of widening of existing diamonds, is consistent with a vanishingly small charging energy of the accidental dot, as has been previously reported in PbTe nanowires [3].

In the absence of charging energy, the g -factor of the dot can be directly inferred from the height in bias voltage of the Zeeman split diamonds, as this height is precisely $E_Z = g\mu_B B$. As an example, the Zeeman-split diamond centered at $V_g \sim -5.8\text{V}$ in Supplementary Fig. 6b gives $E_z \sim 1.6\text{ meV}$, corresponding to $|g| \sim 14$, consistent with previous studies of PbTe quantum dots reported in Refs. [3, 4].

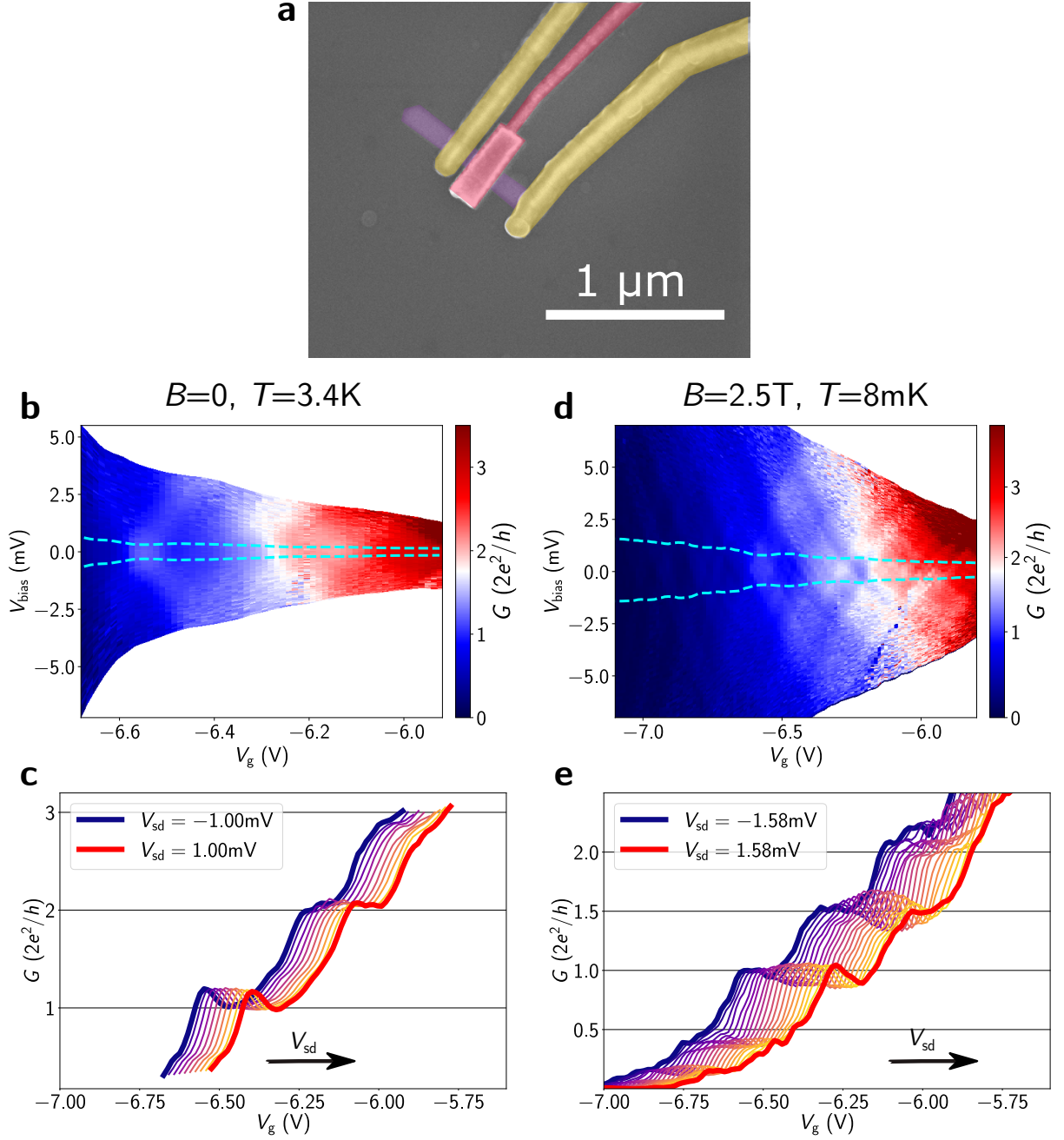
Supplementary Fig. 6c shows the evolution of the quantum dot conductance peaks at a constant voltage bias of $V_{\text{sd}} = 100\mu\text{eV}$ as the out of plane magnetic field is swept from 0 to 2T. We observe that peaks that are degenerate or nearly degenerate at zero field split linearly upon application of field, as expected for spin degeneracy lifted by Zeeman energy in the absence of large charging energy. Additionally, by fixing the external field magnitude at $|B| = 1\text{T}$ and rotating the field in the plane normal to the wire, we see that this Zeeman splitting varies as a function of the angle of the applied magnetic field with minimal (maximal) splitting observed when the field is parallel (perpendicular) to the substrate, as shown in Supplementary Fig. 6d. This is indicative of a highly anisotropic g -factor in the dot, as has been reported in both fully gate-defined [4] and geometrically-defined dots [3]. This is a consequence of a large Rashba-type spin-orbit coupling term tying the g -factor to the anisotropic confining fields present within the wire. As these devices were measured in a cryostat equipped with only a two-axis vector magnet, full determination of the g -factor tensor, as performed in Ref. [4] cannot be made for our accidental dots.

SUPPLEMENTARY REFERENCES

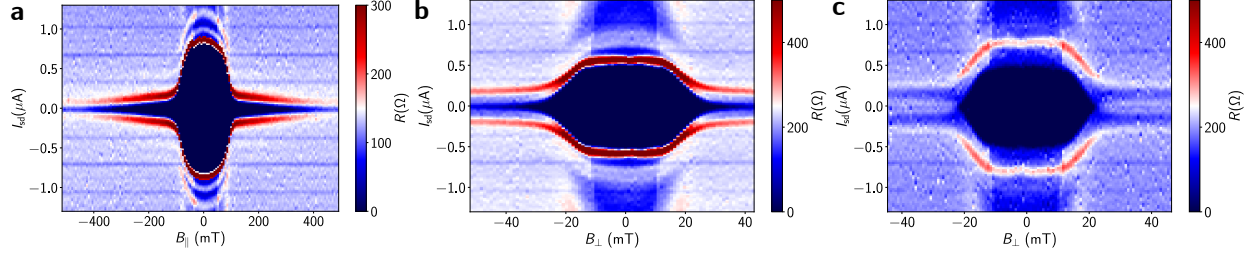
- [1] Jung, J. *et al.* Selective Area Growth of PbTe Nanowire Networks on InP. *Advanced Functional Materials* **32**, 2208974 (2022).
- [2] Mélin, R., Danneau, R. & Winkelmann, C. B. Proposal for detecting the π -shifted cooper quartet supercurrent. *Phys. Rev. Res.* **5**, 033124 (2023).
- [3] Gomanko, M. *et al.* Spin and Orbital Spectroscopy in the Absence of Coulomb Blockade in Lead Telluride Nanowire Quantum Dots. *SciPost Phys.* **13**, 089 (2022).
- [4] ten Kate, S. C. *et al.* Small Charging Energies and g -Factor Anisotropy in PbTe Quantum Dots. *Nano Lett.* **22**, 7049–7056 (2022).



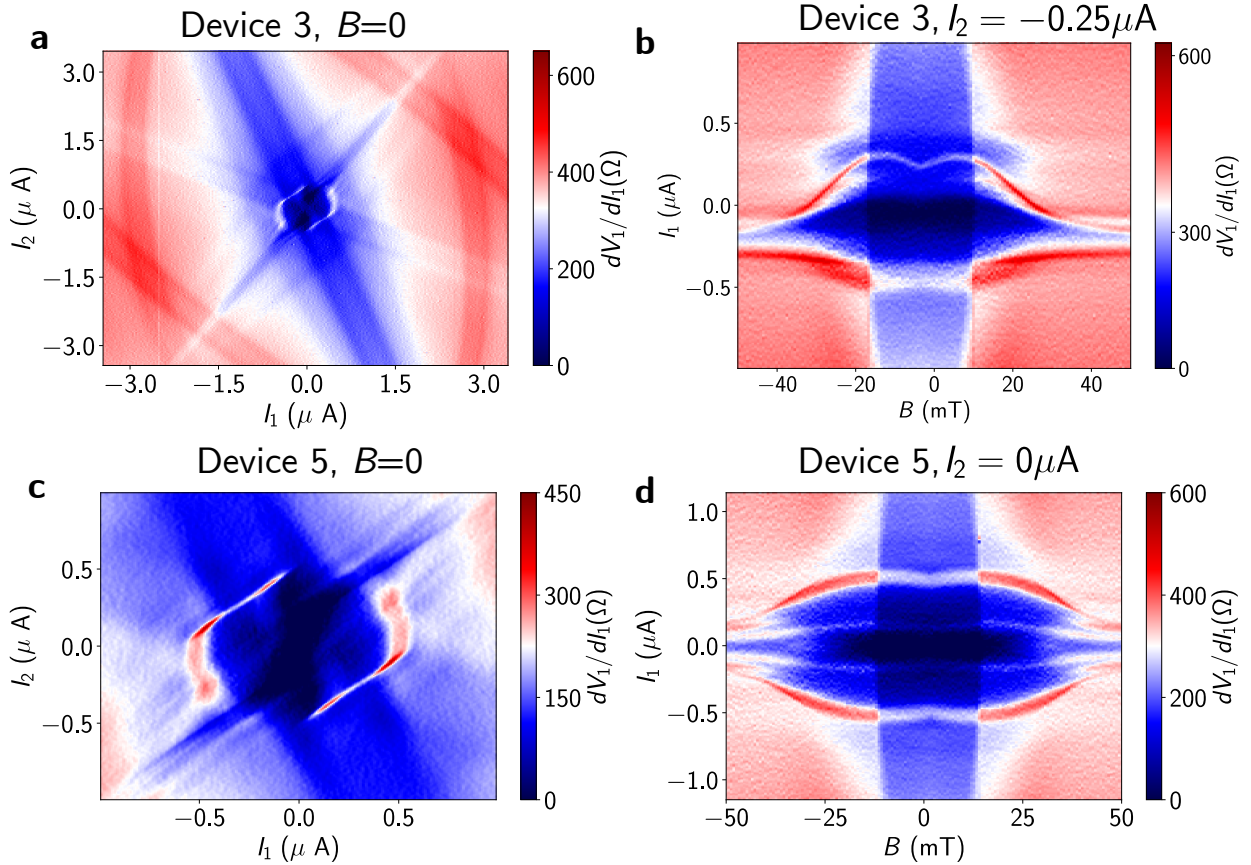
Supplementary Fig. 1. **SEM images of PbTe SAG on an InP(111)A.** Trijunctions intended for 3TJJs (**a-f**) with varying nanowire dimensions and orientations. Specifically, **a** and **d** feature trijunction with arms with a nominal length of 2 μm and a width of 180 nm, while **b** and **e** showcase dimensions of 2 μm length and 120 nm width. **c** and **f** present structures with dimensions of 500 nm length and 90 nm width. Additionally, **g-h** exhibit nanowires with a nominal length of 8 μm and a width of 100 nm, while the nanowire in **i** features a length of 1 μm and a width of 80 nm. Notably, no parasitic growth is observed, with growth confined exclusively to the predefined mask openings. Overall, a wide range of structures and dimensions for PbTe SAG can be obtained, allowing for tailoring to specific applications.



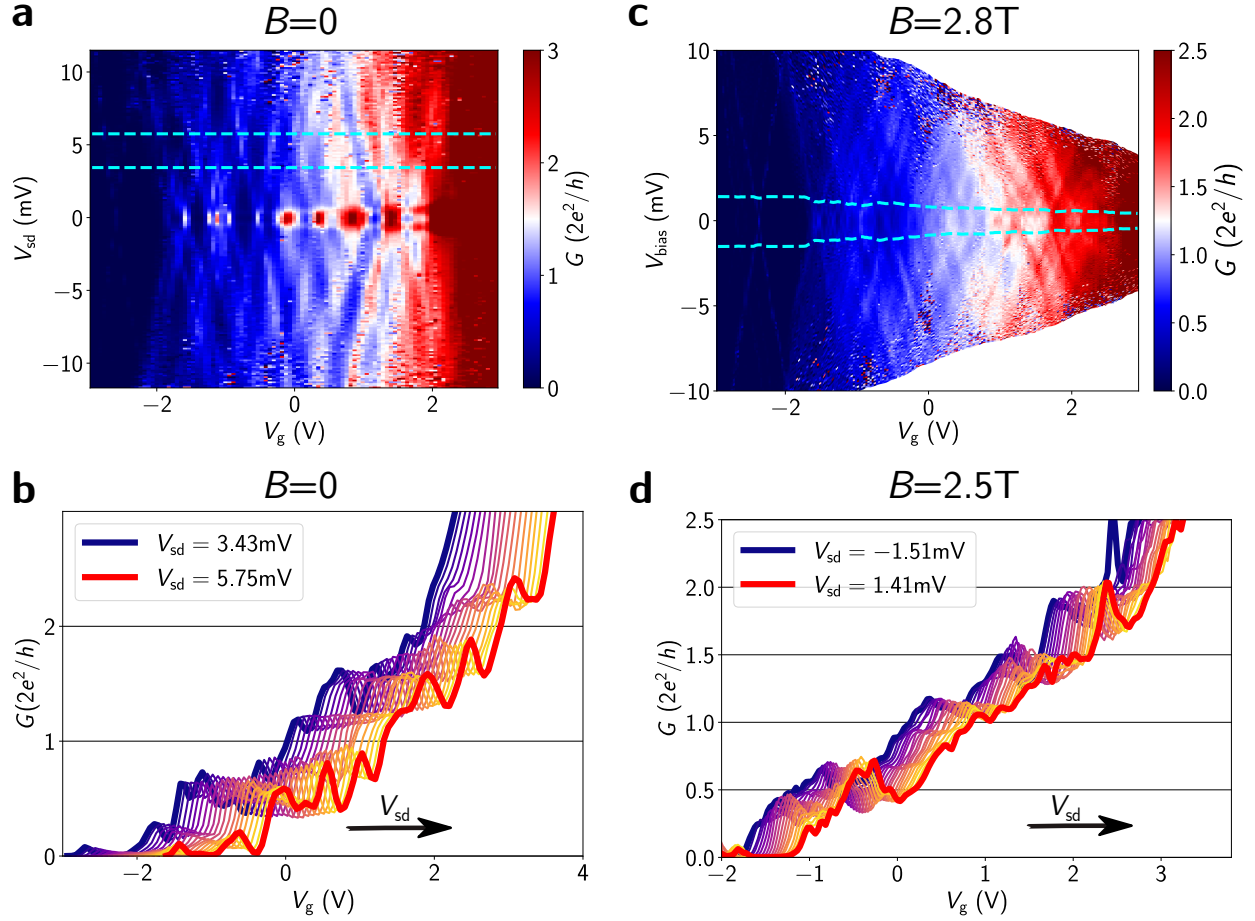
Supplementary Fig. 2. **Quantization with Ti/Au contacts.** **a** False-color scanning electron microscope (SEM) image of the device with Ti/Au Contacts. Conductance as a function of source-drain bias V_{bias} and gate voltage V_g for Device 1 at **b** $B = 0\text{T}$, $T = 3.4\text{K}$ and **d** $B = 2.5\text{T}$, $T = 8\text{mK}$. Conductance as a function of gate voltage for different V_{sd} for **c** $B = 0\text{T}$, $T = 3.4\text{K}$ and **e** $B = 2.5\text{T}$, $T = 8\text{mK}$. The curves correspond to V_{sd} values between **c** -1 mV and 1 mV and **e** -1.58 mV and 1.58 mV (shown dashed cyan lines in panel **b,d**). The curves are each offset along the V_g axis for clarity with an arrow indicating the direction of increasing V_{sd} .



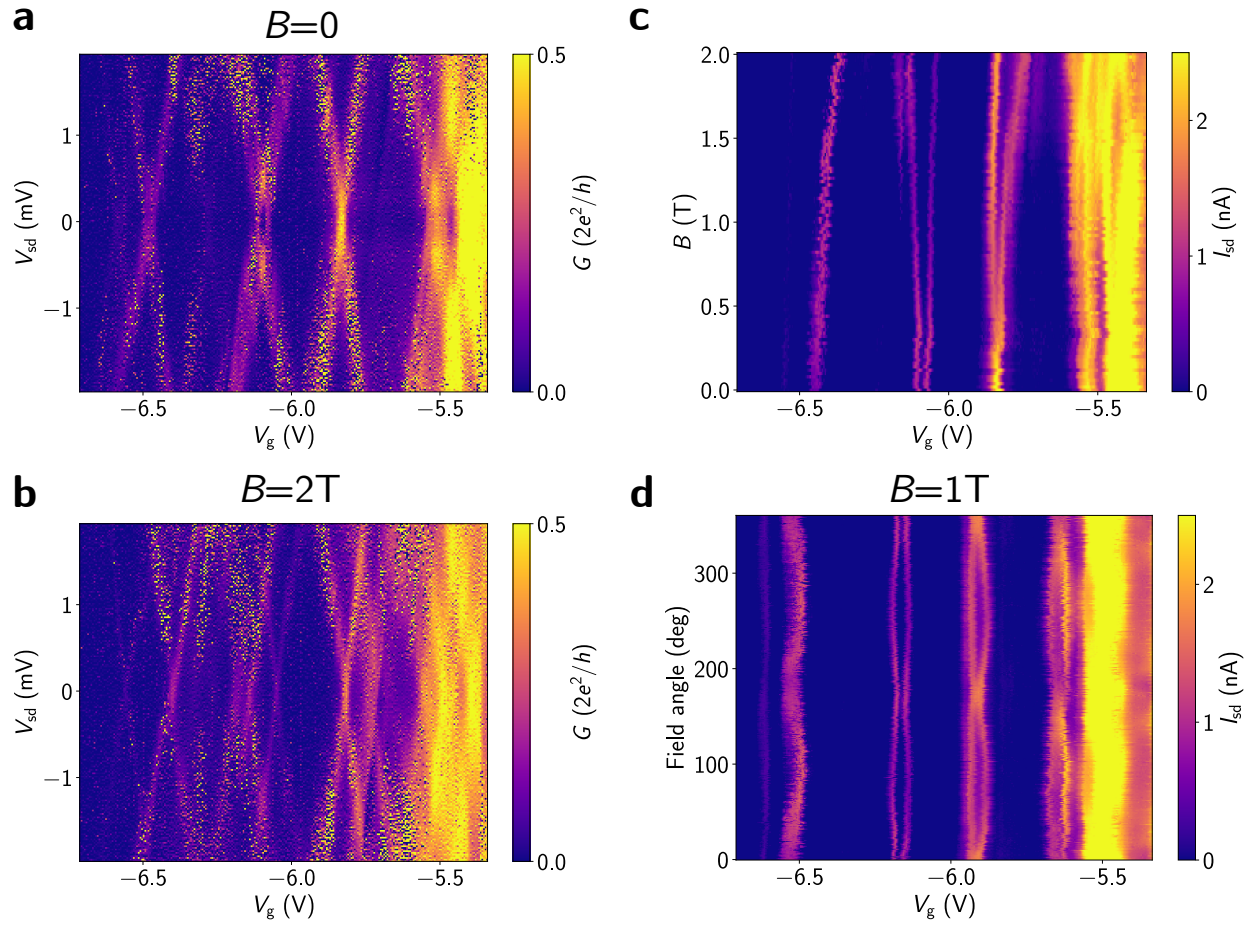
Supplementary Fig. 3. **Fraunhofer patterns.** **a** R as a function of I_{sd} and in-plane magnetic field $B_{||}$ for Device 2. R as a function of I_{sd} and out-of-plane magnetic field B_{\perp} for devices similar to Device 2 with wire diameter **b** 80nm **c** 60nm.



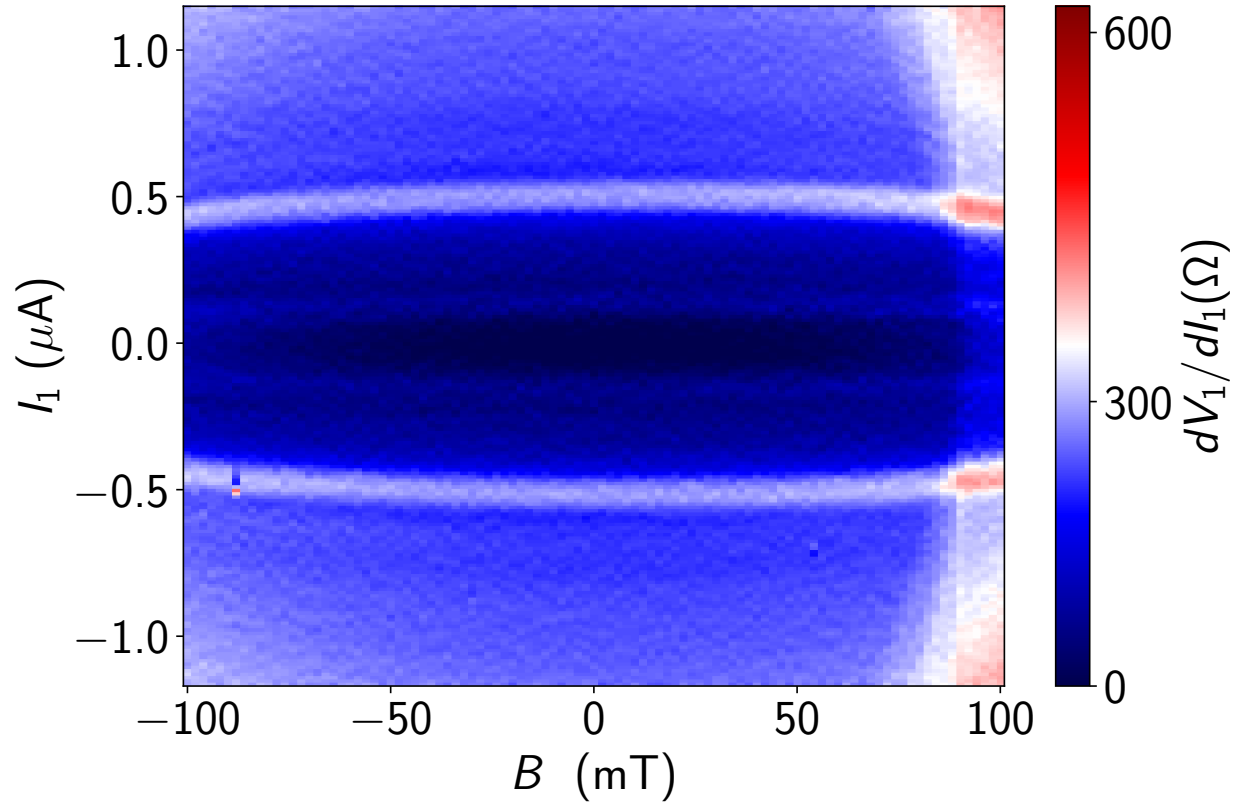
Supplementary Fig. 4. **Three-terminal transport** dV_1/dI_1 as a function of bias currents I_1 and I_2 for **a** Device 3 **c** Device 5. dV_1/dI_1 as a function of I_1 and B **b** for $I_2 = -0.25\mu\text{A}$ for Device 3. **d** for $I_2 = 0\mu\text{A}$ for Device 5.



Supplementary Fig. 5. **Quantization in two-terminal Josephson device.** Conductance as a function of **a** V_{sd} and gate voltage V_g at $B = 0$ T **c** V_{bias} and gate voltage V_g at $B = 2.8$ T . Conductance as a function of gate voltage for different V_{sd} for **b** $B = 0$ T and **d** $B = 2.8$ T. The curves correspond to V_{sd} values between **b** 3.43 mV and 5.75 mV and **d** -1.51 mV and 1.41 mV (shown dashed cyan lines in panel **a,c**). The curves are each offset along the V_g axis for clarity with an arrow indicating the direction of increasing V_{sd} .



Supplementary Fig. 6. **Quantum dot characterization.** Conductance as a function of V_{sd} and gate voltage V_g at **a** $B = 0T$ **b** $B = 2T$. I_{sd} as a function of **c** B and V_g **d** magnetic field angle with the device plane and V_g , magnitude of B is 1T.



Supplementary Fig. 7. **In-plane magnetic field measurement** dV_1/dI_1 as a function of I_1 and B_{\parallel} for Device 3.